LANGMUIR

pubs.acs.org/Langmuir Article

Synthesis and Propulsion of Magnetic Dimers under Orthogonally Applied Electric and Magnetic Fields

Xingrui Zhu, Yan Gao, Ramona Mhana, Tao Yang, Benjamin L. Hanson, Xingfu Yang, Jingjing Gong, and Ning Wu*

Cite This: *Langmuir* 2021, 37, 9151–9161 Read Online

ACCESS | Metrics & More | Article Recommendations | Supporting Information

ABSTRACT: Anisotropic particles have been widely used to make micro/nanomotors that convert chemical, ultrasonic, electrical, or magnetic energy into mechanical energy. The moving directions of most colloidal motors are, however, difficult to control. For example, asymmetric dimers with two lobes of different sizes, ζ-potential, or chemical composition have shown rich propulsion behaviors under alternating current (AC) electric fields due to unbalanced electrohydrodynamic flow. While they always propel in a direction perpendicular to the applied electric field, their moving directions along the substrate are hard to control, limiting their applications for cargo delivery. Inspired by two separate engine and steering wheel systems in automobiles, we use orthogonally applied AC electric field and direct current (DC) magnetic field to control the dimer's speed and direction independently. To this end, we first synthesize magnetic dimers by coating dopamine-functionalized nanoparticles on geometrically asymmetric polystyrene dimers. We further characterize their static and dynamic susceptibilities by measuring the hysteresis diagram and rotation speed experimentally and comparing them with theoretical predictions. The synthesized dimers align their long axes quickly with a planar DC magnetic field, allowing us to control the particles' orientation accurately. The propulsion speed of the dimers, on the other hand, is tunable by an AC electric field applied perpendicularly to the substrate. As a result, we can direct the particle's motion with predesigned trajectories of complex shapes. Our bulk-synthesis approach has the potential to make other types of magnetically anisotropic particles. And the combination of electric and magnetic fields will help pave the way for the assembly of magnetically anisotropic particles into complex structures.

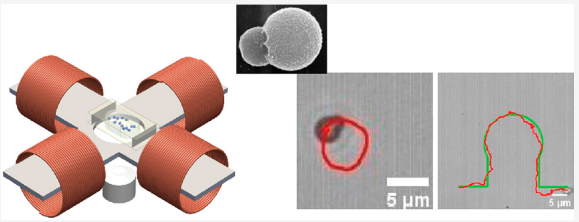

INTRODUCTION

Studies on anisotropic colloidal particles[1] have received considerable attention in recent years due to their potential applications in drug delivery,[2] micro- and nanomachines,[3] colloidal assembly,[4] and particulate emulsifiers.[5] In particular, they have been studied extensively to break the reversibility of low Reynolds number flow and induce locomotion due to their intrinsic asymmetry in geometry, chemical composition, or surface property. Reported particle propulsion mechanisms include self-diffusiophoresis,[6] self-electrophoresis,[7] self-thermophoresis,[8] induced-charge electrophoresis,[9] and electrohydrodynamic flow.[10]

Among many types of anisotropic particles, asymmetric dimers have been proved to be a good candidate for forming chiral structures,[11] planar clusters,[12] photonic materials,[13] and micromotors.[10,11] The dimers typically range from 300 nm to 10 μm in size, making therein situ characterization relatively easy. Under an alternating current (AC) electric field applied perpendicularly to the substrate, we have previously shown that a dimer's linear and circular motion can be achieved due to unbalanced electrohydrodynamic (EHD) flow surrounding the particles. Although the propulsion direction of dimers can be tuned by particle ζ-potential, solution chemistry, and electric field conditions[10] to some extent, precise control of the particle's trajectory remains a challenge. Unlike conventional electrokinetic phenomena where particles move along the direction of either the applied field (e.g., electrophoresis) or field gradient (e.g., dielectrophoresis), EHD micromotors tend to move in directions that are perpendicular to the applied electric field, which is typically normal to the substrate.[10,14] While this provides significant freedom for particle motion along the substrate, its trajectory is random. Similar problems also exist in other colloidal motors driven by nonlinear electrokinetics (such as the propulsion of metallodielectric Janus spheres due to induced charge electroosmosis[9]) and asymmetric chemical reactions.[15,16]

Inspired by the separate systems of engine and steering wheel of automobiles, here we introduce a new method to independently control the propulsion speed and orientation of

Received: May 18, 2021
Revised: July 13, 2021
Published: July 22, 2021

Downloaded via UNIV OF CALIFORNIA SAN DIEGO on January 19, 2024 at 17:52:01 (UTC).
See https://pubs.acs.org/sharingguidelines for options on how to legitimately share published articles.

ACS Publications © 2021 American Chemical Society

https://doi.org/10.1021/acs.langmuir.1c01329
Langmuir 2021, 37, 9151–9161

electrohydrodynamic motors. We propose to orthogonally apply a planar direct current (DC) magnetic field and a normal AC electric field orthogonally. The electric field will generate an unbalanced electrohydrodynamic flow surrounding the asymmetric dimers and provide propulsion power like an engine. On the other hand, the magnetic field, another good candidate for microrobot remote control,[17] can control the dimer's orientation by aligning its long axis, which functions as a steering wheel. Therefore, the dimers should behave like a microcar whose speed and direction can be independently controlled by combining both fields. We also note that electric and magnetic fields are noninvasive and do not require chemical fuels that are usually incompatible with biologically viable media.[18−22]

To achieve this goal, we first synthesize monodisperse magnetic dimers by coating dopamine-functionalized magnetite (Fe_3O_4) nanoparticles on polystyrene dimers whose magnetic susceptibilities are fully characterized and compared with theoretical predictions. Because of the magnetic anisotropy, these dimers respond to both DC and AC magnetic fields for orientation control. Simultaneously, the same dimers are also driven by an AC electric field applied in the orthogonal direction to the planar magnetic field, which controls the propulsion speed. We further show that complex particle trajectories are drawn by preprograming the time sequence of the on/off field conditions.

MATERIALS AND METHODS

Materials. Divinylbenzene (DVB), tetraethyl orthosilicate (TEOS, ≥99.9%), styrene (≥99%), iron(III) chloride hexahydrate (97%), iron(II) chloride tetrahydrate (98%), sodium 4-vinylbenzenesulfonate (≥90%), azobis(methyl propionitrile) (AIBN), sodium dodecyl sulfate (SDS, ≥99.0%), dopamine hydrochloride, and polyvinylpyrrolidone (PVP, M_w = 40 000) were purchased from Sigma-Aldrich. 2,2′-(Diazene-1,2-diyl) bis(2,4-dimethylpentanenitrile) (V65, 95+%) was purchased from Matrix Scientific. 3-(Trimethoxysilyl)propyl methacrylate (TMSPA, stabilized with MEHQ, >93.0%) was purchased from Tokyo Chemical Industry Co. Ammonium hydroxide (NH_4OH, 28−30%) was purchased from VWR Chemicals. Isopropyl alcohol (IPA, 99%) was purchased from Pharmco Aaper.

Synthesis of Polystyrene (PS) Dimers. The polystyrene dimers were synthesized following our previous publication.[23] First, dispersion polymerization was used to make monodisperse PS spheres with 1 μm diameter. After polymerization, the PS particles were washed with water and ethanol and redispersed in deionized (DI) water as 5 wt % colloidal suspensions. After that, an emulsion made from 0.5 mL of 2 wt % SDS, 4 mL of 5 wt % PVP, 0.5 mL of styrene, 50 μL of TMSPA, 50 μL of DVB, and 10 mg of V65 was used to swell 1 mL of PS spheres for 12 h. Afterward, the swollen particles were polymerized and cross-linked at 70 °C for 12 h. The cross-linked polystyrene microsphere seeds (CPS) were washed by DI water twice and ethanol twice with centrifugation. These CPS particles were redispersed in DI water for a second monomer swelling. At this stage, a similar emulsion of PVP, SDS, sodium styrenesulfonate, and V65 with variable amounts of styrene monomer was used to swell the CPS particles overnight. After polymerization at 70 °C for 12 h, the synthesized dimers were washed with DI water and ethanol three times before being redispersed in DI water. The amount of styrene used during the second swelling stage determines the dimer geometry in terms of both aspect ratio and bond length.

Synthesis of Dopamine-Functionalized Magnetite (Fe_3O_4) Nanoparticles. The synthesis of Fe_3O_4 nanoparticles was adopted from An et al.,[24] and we then modified the nanoparticles' surfaces so that they bear positive charges. Bare Fe_3O_4 nanoparticles were prepared by the coprecipitation method from a mixture of $FeCl_2$ and $FeCl_3$ upon the addition of NH_4OH. In a typical synthesis, 0.86 g of $FeCl_2$ and 2.35 g of $FeCl_3$ (1:2 molar ratio) were dissolved into 40 mL of DI water. The mixture was kept under an N_2 atmosphere with vigorous stirring for half an hour. Then, 3.75 mL of 25% NH_4OH was added dropwise to form black precipitates. The solution temperature was then increased to 80 °C under reflux conditions and kept constant for 1 h. The magnetic nanoparticles were then collected by a magnet and washed several times with DI water and redispersed in the same solvent at a concentration of 10 mg/mL. To increase the stability of the Fe_3O_4 nanoparticles, positive surface charges were introduced via a ligand complexation reaction with dopamine hydrochloride. Briefly, 1 g of dopamine hydrochloride was dissolved in 50 mL of the Fe_3O_4 solution and the solution was mixed overnight using a rotator. The mixture was then ultrasonicated for 20 min. The obtained nanoparticles form a very stable colloidal dispersion in water and their ζ-potential is 45 ± 5 mV, as measured by a Zetasizer. The average diameter of magnetic nanoparticles is 19.2 nm, as reported by An et al.[24]

Coating of Fe_3O_4 Nanoparticles on PS Dimers. The positively charged dopamine-functionalized Fe_3O_4 nanoparticles were used to coat negatively charged PS dimers on the basis of electrostatic attraction. Briefly, 4 mL of 10 mg/mL Fe_3O_4−dopamine solution was added to 1 mL of 30 mg/mL dimer solution. The mixture was then stirred overnight, filtered, and washed twice using 1 μm pore filters to remove any excess Fe_3O_4 nanoparticles. The coated dimers were then redispersed in water. To further improve the stability of magnetic dimers, we coated a thin layer of silicon dioxide (<100 nm) on them. Typically, 1 mL of 10 mg/mL dimer solution was first mixed with 0.68 mL of DI water and 3.14 mL of IPA. After mixing, 25 μL of TEOS and 85 μL of NH_4OH were added to the solution. We then sealed the reaction tube and stirred the solution vigorously for 3 h. After the reaction, the silica-coated magnetic dimers were collected by a permanent magnet and washed by DI water three times.

Characterization. The particle morphologies were characterized by scanning electron microscopy (JEOL 700FESEM). ζ-Potential and particle size were measured by a ζ-potential analyzer (ZetaPALS). The synthesized particles have an aspect ratio $R_2/R_1 = 0.67$ and bond length $L/(R_1 + R_2) = 0.61$, where L is the center-to-center distance between two lobes and R_1 (R_2) is the radius of the large (small) lobe. All silica-coated magnetic dimers are negatively charged with a ζ-potential of −45 ± 4 mV. The magnetic hysteresis diagrams and FC−ZFC curves were obtained by a superconducting quantum interference device (SQUID) magnetometer (Quantum Design MPMS3). Particles were dried overnight, and their weights were measured. The powders were then placed on a holder and inserted into the SQUID magnetometer (Quantum Design MPMS3). The magnetic field increased from 0 to 1 T, gradually decreased to −1 T, and then increased to 0 T, with 1 mT increments between −0.1 T and 0.1 T and 30 mT increments over other regimes.

Electric and Magnetic Fields Setup. Our experimental setup is shown in Figure 1. To enable linear and rotational motion of particles, we applied a sinusoidal AC electric field using an AC function generator (RIGOL DG4062) connected between the top and bottom electrodes (ITO-coated glass slides, Delta Technologies Limited, 25 × 75 × 1.1 mm, 70−100 Ω) that were separated by two 100-μm-thick polymeric spacers. The magnetic field was generated through four air-cored copper solenoid coils of 50 mm inner diameter, 51 mm length, and 400 turns with a current capacity of 3.5 A, installed into an acrylic crossing board. Each coil was connected to a DC or AC function generator, which was controlled by a custom Matlab (MathWorks Inc.) program with an output card (National Instruments, NI-9263). Real-time current measurement for each coil was obtained via a data acquire card (NI USB-6009) by measuring the voltage across a serially connected 1 Ω resistor (ARCOL, HS150 1RF). The magnetic field strength was measured by a Gauss meter (AlphaLab Inc., VGM786). To generate the circularly rotating magnetic field, 50 Hz AC currents were applied to four coils. The phase lag between neighboring coils is ±90° so that both clockwise and counterclockwise rotational magnetic fields can be generated.

Under an optical microscope (Olympus IX 71), both the linear and rotational motions of magnetic dimers were recorded by a black/white camera (EPIX SV643M) with 30 frames/s. The particle's center of mass was identified by Matlab. By analyzing the movement of the dimer's

https://doi.org/10.1021/acs.langmuir.1c01329
Langmuir 2021, 37, 9151−9161

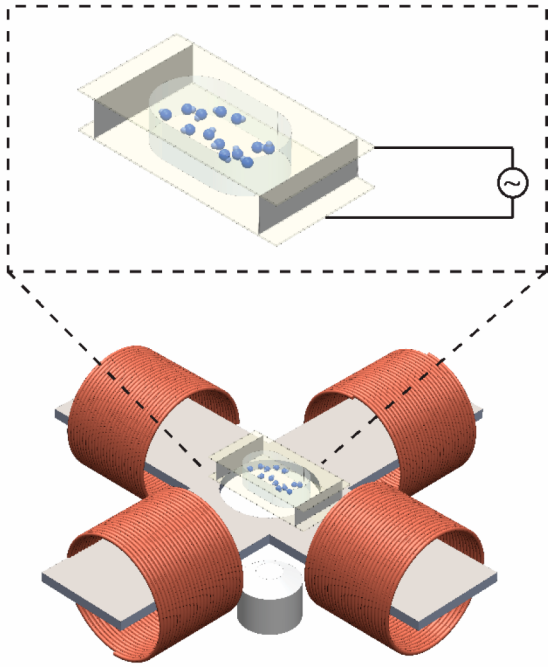

Figure 1. Experiment setup for controlling the linear and rotational motion of magnetic dimers under orthogonally applied electric and magnetic fields. The range of the electric field used is 4−20 V peak-to-peak (V_{pp}) and 400−1000 Hz, and the range of magnetic field applied is 0.83−5.22 mT and 0−50 Hz.

center of mass and the orientation of its long axis using ImageJ, both linear propulsion velocity and angular frequency were obtained.

RESULTS AND DISCUSSION

Synthesis of Magnetic Dimers. Our synthetic route is illustrated in Figure 2. The PS dimers were made on the basis of

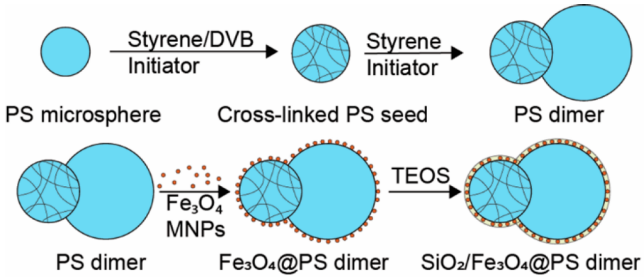

Figure 2. Schematic for the synthesis of magnetic dimers.

the two-step emulsion polymerization method reported before,[25] where cross-linked polystyrene seed particles were synthesized first. The second lobe is then generated via swelling the cross-linked seeds by styrene and sodium styrenesulfonate monomers again. Since polystyrene chains are cross-linked within the seeds, the elastic energy penalty prohibits further swelling of the seeds. As a result, styrene partially wets the seed particle and forms a second lobe on it. Due to the addition of sodium styrenesulfonate, the synthesized PS dimers were negatively charged (ζ-potential = −40 ± 5 mV). The Fe_3O_4 nanoparticles functionalized with dopamine (having positive ζ-potentials) were then electrostatically adsorbed onto the PS dimers. To further enhance the particle stability and electrohydrodynamic propulsion, a thin film of silica (<100 nm) was coated by the sol−gel reaction of TEOS in IPA catalyzed by NH_4OH.

The SEM images of bare PS dimers, dimers coated with magnetite nanoparticles (Fe_3O_4@PS), and magnetic dimers with an additional silica layer (SiO_2/Fe_3O_4@PS) are shown in Figure 3. The Fe_3O_4 nanoparticles, indicated by dots in the inset of Figure 3b, are uniformly distributed on the initially smooth (dark gray) PS dimer surfaces. The rough surface morphology of magnetic dimers is preserved after silica coating (Figure 3c), which was grown by heterogeneous nucleation on Fe_3O_4 particles. The energy-dispersive X-ray spectroscopy (EDX) in Figure 3d−f further confirms that the particles are rich in silicon and iron signals (the copper signal comes from the copper substrate for SEM sample preparation). This sequential coating of Fe_3O_4 via electrostatic adsorption and coating SiO_2 via TEOS nucleation can be extended to other types of particles. For example, we have also made SiO_2/Fe_3O_4@PS microspheres by coating Fe_3O_4 nanoparticles on PS microspheres. Our bulk synthesis strategy can produce magnetic particles with uniform surface properties and narrow polydispersity, crucial for scientific studies and engineering applications.

As shown in Figure S1 of the Supporting Information (SI), the surface of a bare PS dimer is smooth, while nanoparticles cover the Fe_3O_4@PS dimer, and the SiO_2/Fe_3O_4@PS dimer surface has rough spikes. To estimate the silica layer thickness, EDS mapping of the SiO_2/Fe_3O_4@PS dimer was obtained (Figure S2, SI). The results show that the carbon, iron, and silicon weight ratio is 27.6:0.43:0.3. Each dimer has a volume of 8.6×10^{-18} m^3 and surface area of 18.53×10^{-12} m^2. Therefore, the weight of a PS dimer is 9.116×10^{-15} kg (ρ_{PS} = 1060 kg/m^3). On the basis of the elements' weight ratio, the weight of silica is ~2.80×10^{-16} kg. The total volume of silica is ~1.21×10^{-19} m^3 (ρ_{SiO_2} = 2320 kg/m^3). Assuming that the surface coating is uniform, the silica layer is about 6.5 nm.

The stability of colloidal particles is an essential characteristic for particles with a surface coating. Although the Fe_3O_4@PS dimers are stable in dilute aqueous solutions, they tend to aggregate in high particle concentrations due to their relatively small net surface charges, since the Fe_3O_4 nanoparticles are positively charged and pristine PS dimers are negatively charged. In comparison, the SiO_2/Fe_3O_4@PS dimers can be suspended in high concentrations without any noticeable aggregation. The enhanced stability can be attributed to the additional negatively charged silica layers. Recently, a method to synthesize submicron magnetic ellipsoids and dumbbells via layer-by-layer (LBL) adsorption[26] was reported. In order to increase the number of surface charges, both anionic and cationic polyelectrolytes were coated onto the particle surface, forming a polyelectrolyte matrix so that negatively charged magnetic nanoparticles can be electrostatically adsorbed. Here, we purposely synthesize positively charged magnetic nanoparticles because our PS dimers are negatively charged. Compared to the LBL method, we eliminate multiple steps of forming layers of polyelectrolytes while maintaining good particle stability.

Characterization of the Magnetic Properties of Dimers. To characterize the magnetic properties of our synthesized particles, we measure their magnetization hysteresis with a vibrating sample magnetometer (VSM) at 298 K, as shown in Figure 4a−c. For comparison, we also show the magnetic hysteresis diagrams for commercially available Dynabeads of similar sizes (adapted from ref 27) in Figure 4d. Figure 4a indicates that the saturation magnetization of Fe_3O_4

https://doi.org/10.1021/acs.langmuir.1c01329
Langmuir 2021, 37, 9151−9161

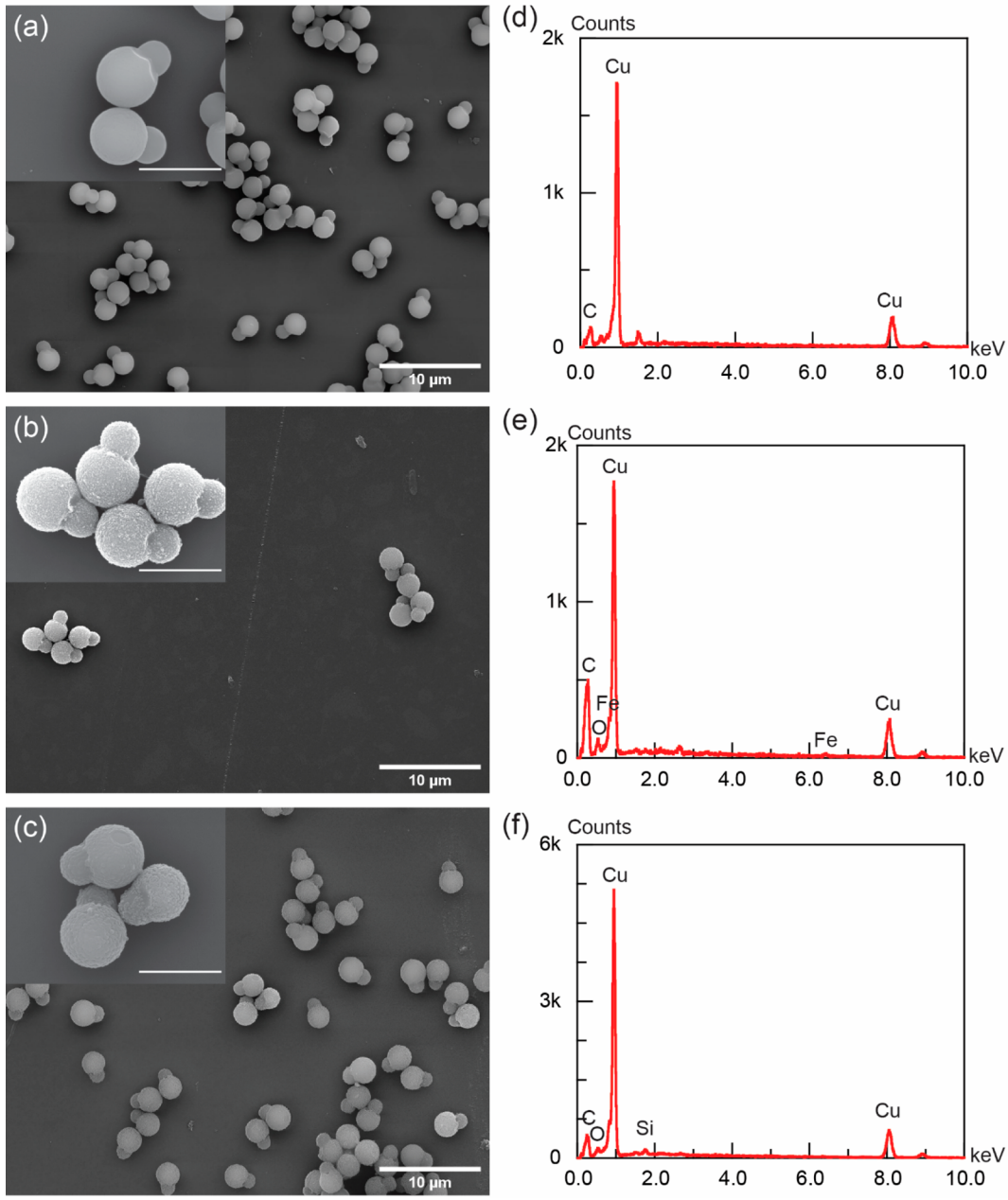

Figure 3. SEM images of (a) bare PS dimers, (b) Fe_3O_4@PS dimers, and (c) SiO_2/Fe_3O_4@PS dimers. Inset scale bars: 3 μm. Their EDX analyses are shown in parts d–f.

nanoparticles is 35 A m^2/kg, which represents the maximum magnetic response of particles. It is slightly smaller than those (40–60 A m^2/kg) reported by other synthesis methods.[28] This may be attributed to the surface functionalization with dopamine hydrochloride, which pins the surface spin and leads to the reduction of magnetization, as observed in other types of surface-modified Fe_3O_4 nanoparticles.[29] Both Fe_3O_4@PS and SiO_2/Fe_3O_4@PS dimers are superparamagnetic since nearly zero (<0.223 A m^2/kg) remnant magnetization can be seen (see the inset of Figure 4b). The magnetic PS dimers exhibit smaller magnetization after coating with a thin layer of silica. This is caused by the spin disorder surface effects,[30] commonly observed in magnetite nanoparticles coated by a thin layer of nonmagnetic materials such as polymer or silica. Briefly, the intimate contact between magnetite and the silica coating suppresses the spin movement at the interface, so the magnetic dipoles generated in each Fe_3O_4 nanoparticle cannot be fully aligned with the external field, leading to spin disorder and a lowered saturation magnetization.[31] They also have smaller saturation values than Fe_3O_4@PS spheres (Figure 4b,c). The reason could be ascribed to the smaller surface area of dimers than PS seeds when they have the same mass. Figure 4d shows the hysteresis diagram of commercially available Dynabeads M-270 (2.7 μm in diameter) and M-450 (4.5 μm in diameter) with saturation magnetization, M_{sat}, of 10.3 and 18.5 A m^2/kg, respectively. These values are a few times larger than our Fe_3O_4@PS spheres since Dynabeads have magnetic nanoparticles embedded inside the PS matrix, while our magnetic nanoparticles are only coated on the surface. In addition, superparamagnetism can be characterized by the FC–ZFC measurement (Figure S3, SI). We obtain the blocking temperature of 80.8, 57.7, 80.1, and 115 K for Fe_3O_4

https://doi.org/10.1021/acs.langmuir.1c01329
Langmuir 2021, 37, 9151–9161

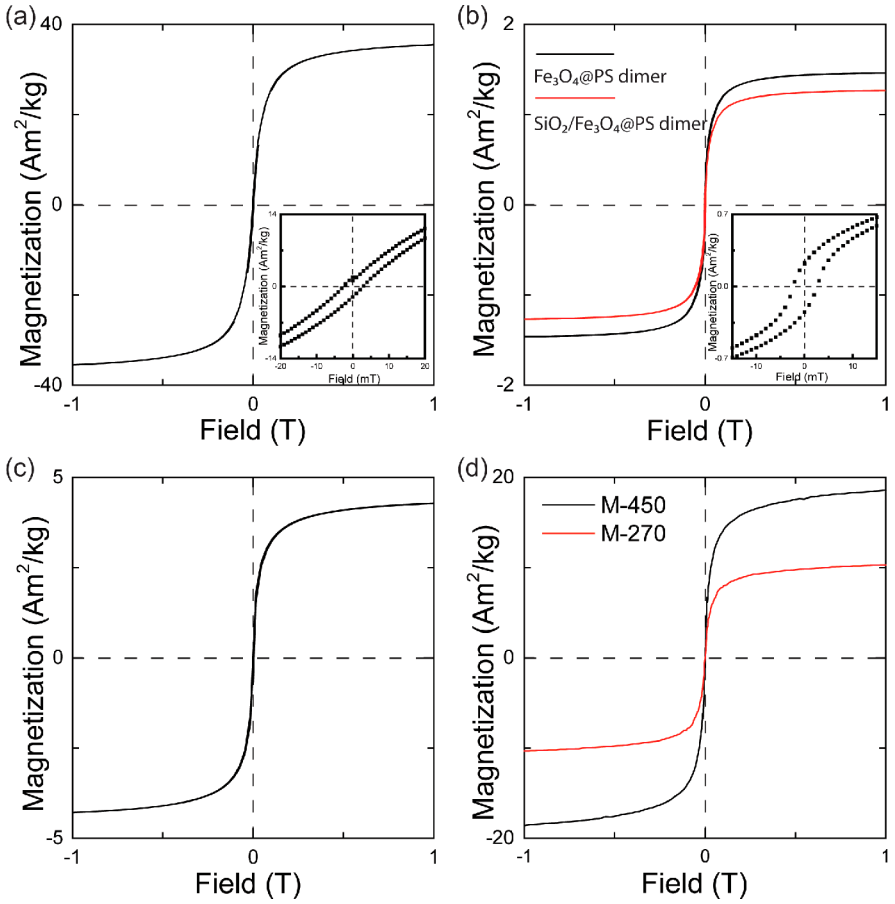

Figure 4. Magnetic hysteresis diagrams of (a) Fe_3O_4 nanoparticles, (b) Fe_3O_4@PS dimers and SiO_2/Fe_3O_4@PS dimers, (c) Fe_3O_4@PS spheres, and (d) commercially available magnetic spheres of 2.7 and 4.5 μm (Dynabeads M-270 and M-450), which is adapted from ref 27 (copyright 2005 Elsevier B.V.) with permission.

nanoparticles, Fe_3O_4@CPS dimers, Fe_3O_4@PS dimers, and SiO_2/Fe_3O_4@PS dimers, respectively, under 100 Oe DC field. All of these blocking temperatures are well below room temperature. This proves that our particles are superparamagnetic at room temperature.

In addition to saturation magnetization, the hysteresis diagram also allows us to obtain the static magnetic mass susceptibility, $\chi_{0,m}$, of particles based on the Langevin function[32]

$$M = Nm_{np}\left[\coth\left(\frac{\mu_0 m_{np} H}{k_B T}\right) - \frac{k_B T}{\mu_0 m_{np} H}\right] \quad (1)$$

where M is the dimer magnetization, N is the number of Fe_3O_4 nanoparticles, m_{np} is the magnetic moment of one single nanoparticle, μ_0 is the vacuum permeability, k_B is the Boltzmann constant, and T is the temperature. When $\frac{\mu_0 m_{np} H}{k_B T} \ll 1$, $M = \chi_{0,m} H \approx \frac{N\mu_0 {m_{np}}^2 H}{3k_B T}$. For Fe_3O_4 nanoparticles, $\chi_{0,m} = 8.17 \times 10^{-4}$ m^3/kg. For Fe_3O_4@PS dimers and SiO_2/Fe_3O_4@PS dimers, their susceptibilities reduce to 8.65×10^{-5} and 8.25×10^{-5} m^3/kg, respectively. For comparison, the susceptibilities of commercial Dynabeads M-280 and M-450 are 5.4×10^{-4} and 1.02×10^{-3} m^3/kg, respectively,[27] about 5−10 times larger than our dimers. Again, this can be attributed to the composite nature of Dynabeads, in which Fe_3O_4 loading is much higher.

The percentage surface coverage of Fe_3O_4 nanoparticles on dimers can also be estimated from the hysteresis diagram. When $\frac{\mu_0 m_{np} H}{k_B T} \gg 1$, $M \approx M_{sat} = Nm_{np}$. So

$$\chi_{0,m} = \frac{M}{H} = \frac{N{m_{np}}^2 \mu_0}{3k_B T} = \frac{{M_{sat}}^2 \mu_0}{3Nk_B T} \quad (2)$$

With the measured saturated magnetization M_{sat} and susceptibility $\chi_{0,m}$, we find that the maximum magnetization for each magnetic nanoparticle is 6.47×10^{-19} A m^2, which leads to 1.156×10^{-14} A m^2 per dimer. Therefore, we estimate that there are ~17 867 Fe_3O_4 nanoparticles on one SiO_2/Fe_3O_4@PS dimer. By further assuming that the magnetic nanoparticles' size is ~19−25 nm, we estimate that the nanoparticle surface coverage on dimers is ~29−40%.

Dimer Rotation under a Planar Rotating Magnetic Field. To further understand the magnetic response of dimers, we characterized their rotation under a circularly rotating magnetic field along the x−y-plane; i.e., $H = H_0 e^{i\omega_M t}(\hat{x} - i\hat{y})$, where H_0 is the field strength and $\omega_M = 2\pi f_M$ is the angular frequency. Qualitatively, the dimers rotate in the same direction as the applied field, i.e., clockwise (counterclockwise) rotation under a clockwise (counterclockwise) rotating field, as shown in SI Movie 1 (SI). Quantitatively, Figure 5a shows that the rotation behavior of SiO_2/Fe_3O_4@PS dimers can be categorized into three different regimes under a constant field strength. At low frequencies, the dimers rotate synchronously with the field. Above a critical frequency ω_c, its rotational speed decreases

https://doi.org/10.1021/acs.langmuir.1c01329
Langmuir 2021, 37, 9151−9161

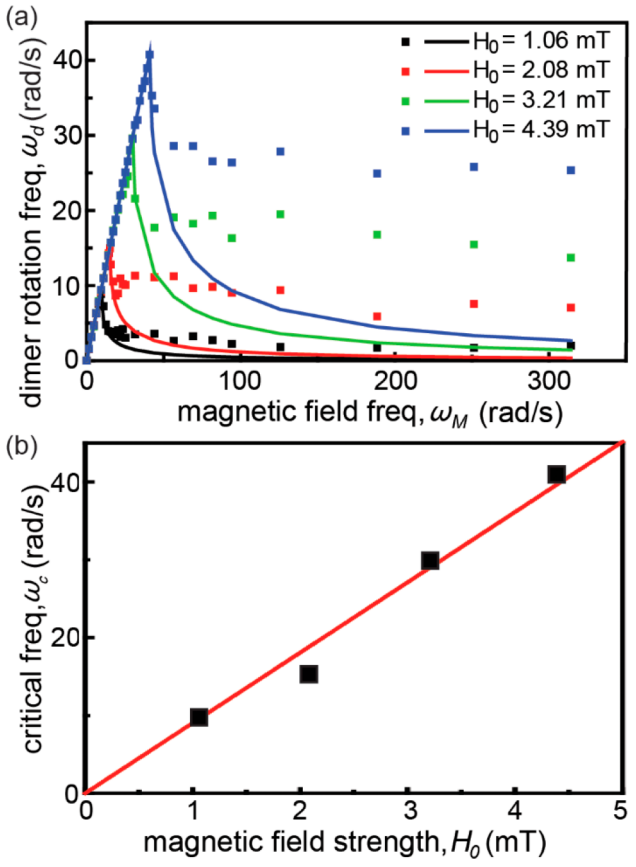

Figure 5. (a) The angular rotational frequency of SiO_2/Fe_3O_4@PS dimers under different field strengths and frequencies. The solid lines are predictions from eq 10. (b) The critical rotation frequency ω_c under different magnetic field strengths. The solid line represents a linear fitting.

quickly. For the same dimer, the critical frequency ω_c is proportional to the field strength H_0 (Figure 5b). As frequency increases further, the dimer rotates at a relatively constant speed. For example, when $\omega_M = 100\pi$ rad/s, the angular rotating frequency of SiO_2/Fe_3O_4@PS dimers, ω_d, is proportional to the field strength squared (Figure 6). For comparison, we also

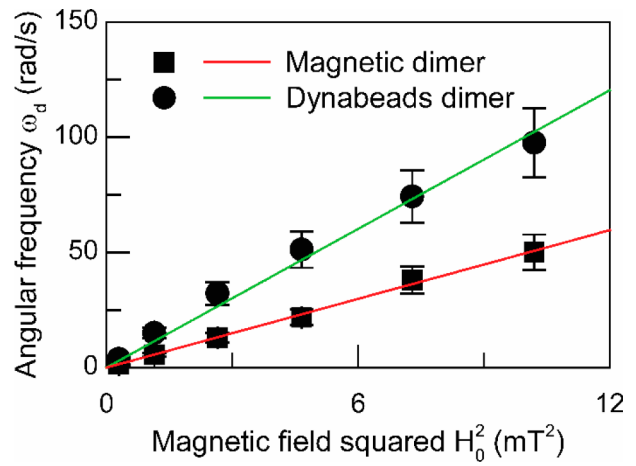

Figure 6. Angular rotation frequency of SiO_2/Fe_3O_4@PS dimers and Dynabeads dimers under different magnetic field strengths. Two straight lines are linear fittings with zero intercept.

assembled 4.5 and 2.7 μm Dynabeads into asymmetric dimers under the same rotating magnetic field. Their angular velocity is about twice that of our synthesized dimers. Interestingly, we find that ω_d is ~50% larger for Fe_3O_4@PS dimers than SiO_2/Fe_3O_4@PS dimers due to the lack of the silica layer's pinning effect.

To understand the dimer rotation, we need to know the dynamic response of magnetic particles under an AC magnetic field. In general, the magnetic relaxation of particles has contributions from both Brownian relaxation (reorientation of magnetic dipole due to Brownian rotation) and Néel relaxation (magnetic dipole flips between two preferred orientations under the influence of temperature).[33] For complex volume susceptibility $\chi = \chi' - i\chi''$, the real part (in-phase component) χ' and imaginary part (out-of-phase component) χ'' are related to the static volume susceptibility χ_0 by[34]

$$\chi' = \frac{\chi_0}{1 + (\omega_M\tau)^2} \quad \text{and} \quad \chi'' = \frac{\omega_M\tau\chi_0}{1 + (\omega_M\tau)^2} \tag{3}$$

where τ is the effective relaxation time contributed by both Brownian and Néel relaxation times τ_B and τ_N:

$$\frac{1}{\tau} = \frac{1}{\tau_B} + \frac{1}{\tau_N} \tag{4}$$

$$\tau_B = \frac{3\eta V_H}{k_B T} \quad \text{and} \quad \tau_N = \tau_0 \exp\left(\frac{KV_n}{k_B T}\right) \tag{5}$$

where V_H is the hydrodynamic volume of the magnetic dimer, τ_0 is a relaxation time constant ~10^{-9} s, K is the anisotropy constant, which depends on material composition and particle geometry,[35,36] η is the fluid viscosity, and V_n is the volume of a single magnetic nanoparticle. Note that Néel relaxation time τ_N is very sensitive to the anisotropy constant K because of the exponential term. According to Fannin et al.,[37] K for magnetite particles is between 13.35 and 14.28 kJ/m^3. For convenience, we choose K = 14 kJ/m^3. By plugging $\omega_M = 100\pi$ rad/s and $\chi_{0,m}$ = 8.25×10^{-5} m^3/kg (obtained from the hysteresis diagram) into eqs 3–5, we obtain the estimations of the mass susceptibilities $\chi_m' = 8.01 \times 10^{-5}$ m^3/kg and $\chi_m'' = 1.37 \times 10^{-5}$ m^3/kg. In the following, we will use these values to probe the origin of the magnetic torques on our dimers.

As shown in Figure 7a, a torque can arise from the dimer's *permanent dipole*, $m_p = m_{p1} + m_{p2}$, which maintains a constant angle with the rotating magnetic field,

$$T_{M,p} = m_p \times \mu_0 H = m_p \mu_0 H_0 \sin(\theta_M - \theta_d)\hat{z} \tag{6}$$

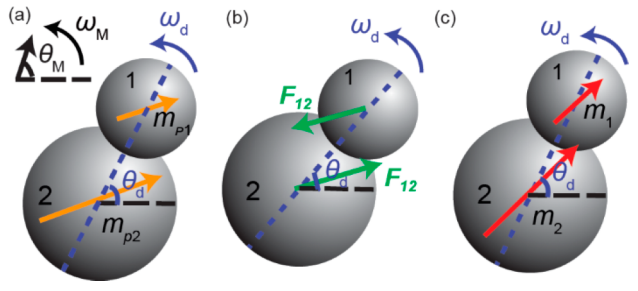

Figure 7. Schematic showing the torque on dimers due to (a) permanent magnetic moment (orange), (b) interaction (green) between field-induced dipoles, or (c) phase lag between induced dipoles (red) and field.

https://doi.org/10.1021/acs.langmuir.1c01329
Langmuir 2021, 37, 9151−9161

where $\theta_M = \omega_M t$ and $\theta_d = \omega_d t$ are the instantaneous field and dimer angles, respectively. The magnetic torque is balanced by the hydrodynamic torque, which can be approximated by[22,38]

$$T_h = -C\pi\eta(R_1 + R_2)^3 \frac{d\theta_d}{dt}\hat{z} \tag{7}$$

We chose $C = 10$ for a dimer, which is very close to the value obtained from numerical modeling.[39] Letting $T_{M,p} + T_h = 0$,[22] one obtained a relationship between the dimer's angular frequency and field frequency:

$$\frac{d\theta_d}{dt} = \omega_{c,p}\sin(\theta_M - \theta_d) \quad \text{and} \quad \omega_{c,p} = \frac{m_p\mu_0 H_0}{C\pi\eta(R_1 + R_2)^3} \tag{8}$$

If we let $\phi = \theta_M - \theta_d = \omega_M t - \theta_d$, eq 8 can be rewritten as

$$\frac{d\phi}{dt} = \omega_M - \omega_{c,p}\sin\beta \tag{9}$$

Equation 9 is an example of the nonuniform oscillator equation,[40] and its characteristics can be summarized by the following. When $\omega_M \le \omega_{c,p}$, the dimer's rotation frequency $\omega_d = \omega_M$; i.e., it rotates synchronously with the applied field and the constant phase angle $\phi = \phi_0 = \sin^{-1}\left(\frac{\omega_M}{\omega_{c,p}}\right)$. When $\omega_M > \omega_{c,p}$, the period-average angular frequency

$$\omega_d = \left\langle \frac{d\theta_d}{dt} \right\rangle = \omega_M - \sqrt{\omega_M^2 - \omega_{c,p}^2} \tag{10}$$

i.e., its rotation speed decays to zero as the field frequency increases.

A second possible source of the magnetic torque is from the interaction between *field-induced dipoles* on two lobes. As shown in Figure 7b, we consider a dimer as two tangentially connected magnetic spheres of radii R_1 and R_2. The force between two spheres F_{12} has components in both $\hat{r}$ and $\hat{\theta}$ directions. The torque is, however, only generated from the $\hat{\theta}$ component force, which can be expressed as

$$F_\theta = \frac{3\mu_0 m_1 m_2}{4\pi(R_1 + R_2)^4}\sin[2(\theta_M - \theta_d)]\hat{\theta} \tag{11}$$

We further assume that the induced magnetic dipole moment m_i is proportional to the volume V_i of sphere i; i.e., $m_i = \chi V_i H = \frac{4\pi R_i^3(\chi' - i\chi'')H}{3}$. Notice that χ here is the volume susceptibility, different from χ_m, the mass susceptibility. After substituting both m_i and H into eq 11 and taking the time average over one period of the rotation field, we have

$$\langle F_\theta \rangle = \frac{4\pi\mu_0 R_1^3 R_2^3 H_0^2 \sin[2(\theta_M - \theta_d)](\chi'^2 + \chi''^2)}{3(R_1 + R_2)^4} \tag{12}$$

The magnetic torque due to induced dipolar interactions can then be obtained:

$$T_{M,d} = \langle F_\theta \times (R_1 + R_2)\hat{r}\rangle = \frac{4\pi\mu_0 R_1^3 R_2^3 H_0^2 \sin[2(\theta_M - \theta_d)](\chi'^2 + \chi''^2)}{3(R_1 + R_2)^3}\hat{z} \tag{13}$$

The balance between $T_{M,d}$ and T_h leads to

$$\frac{d\theta_d}{dt} = \omega_{c,i}\sin[2(\omega_M t - \theta_d)] \quad \text{and} \quad \omega_{c,i} = \frac{4\mu_0 R_1^3 R_2^3 H_0^2(\chi'^2 + \chi''^2)}{3C\eta(R_1 + R_2)^6} \tag{14}$$

If we let $\beta = \theta_M - \theta_d = \omega_M t - \theta_d$, eq 14 can be rewritten as

$$\frac{d\beta}{dt} = \omega_M - \omega_{c,i}\sin 2\beta \tag{15}$$

Note that eq 15 is similar to eq 9. Therefore, just like the dimer's rotation caused by permanent dipoles, the induced dipolar interaction will also cause the dimer to rotate synchronously with the field when $\omega_M \le \omega_{c,i}$, and its speed will decay to zero when $\omega_M > \omega_{c,i}$. At first glance, both mechanisms are qualitatively consistent with our experimental observation in Figure 5a. However, these two mechanisms predict different scaling between the critical frequency ($\omega_{c,p}$ or $\omega_{c,i}$) and field strength H_0 according to eqs 8 and 14. The fact that the maximum dimer rotation speed is proportional to the field strength (Figure 5b) supports the hypothesis that permanent dipoles on the dimers control their rotation at low frequencies. Moreover, by fitting Figure 5b with eq 8 for $\omega_{c,p}$, we obtain a permanent dipole of 2.08×10^{-15} A m^2 per dimer, close to the remnant dipole (2.03×10^{-15} A m^2 per dimer) measured in the hysteresis diagrams (inset of Figure 4b). On the other hand, the solid curves based on eq 10 in Figure 5a underpredict the dimer's rotation speed when $\omega_M \gg \omega_{c,p}$, which reaches a plateau instead of decaying to zero. This inconsistency points to a different mechanism for dimer rotation at high frequencies.

The third possible mechanism for dimer rotation at high frequencies is due to the *phase lag* between induced dipoles on each sphere and the applied field (Figure 7c), i.e.,

$$T_{M,i} = \langle m_1 \times \mu_0 H + m_2 \times \mu_0 H\rangle \tag{16}$$

By substituting $m_i = \frac{4\pi R_i^3(\chi' - i\chi'')H}{3}$ and $H = H_0 e^{i\omega_M t}(\hat{x} - i\hat{y})$ into eq 16 and taking the time average over one period of rotation, we have

$$T_{M,i} = \frac{4\pi\mu_0(R_1^3 + R_2^3)H_0^2\chi''}{3}\hat{z} \tag{17}$$

The balance of $T_{M,i}$ and T_h yields another expression for the dimer's rotational frequency

$$\omega_d = \frac{4\mu_0(R_1^3 + R_2^3)H_0^2\chi''}{3c\eta(R_1 + R_2)^3} \tag{18}$$

Note that eq 18 predicts that ω_d is proportional to both χ'' and H_0^2. The dependence of ω_d on field strength squared at high frequencies (e.g., $\omega_M = 314$ rad/s) is consistent with the data shown in Figure 6. Furthermore, by fitting the data with eq 18, we estimate that $\chi_m'' \sim 7.08 \times 10^{-5}$ m^3/kg, on the same order of χ_m'' (1.37×10^{-5} m^3/kg) inferred from the hysteresis diagram. In comparison, we assume that the dimer rotation when $\omega_M \gg \omega_{c,p}$ is due to the interaction between induced dipoles. By fitting the data with eq 14, we obtained $\chi_m' \sim 2.9 \times 10^{-3}$ m^3/kg, which is 2 orders of magnitude larger than χ_m' (8.01×10^{-5} m^3/kg) derived from the above-mentioned hysteresis diagram. Overall, we conclude that dimer rotation is primarily driven by the permanent dipoles when $\omega_M \le \omega_{c,p}$ and the phase lag between the induced dipoles and field when $\omega_M \gg \omega_{c,p}$.

https://doi.org/10.1021/acs.langmuir.1c01329
Langmuir 2021, 37, 9151−9161

Propulsion of Magnetic Dimers under AC Electric Fields. After characterizing the dimers' magnetic properties, we further test their propulsion behavior under an applied AC electric field along the *z*-direction. SI Movie 2 shows that the dimer propels laterally on the substrate with its small lobe leading forward. Figure 8 shows that the propulsion speeds of

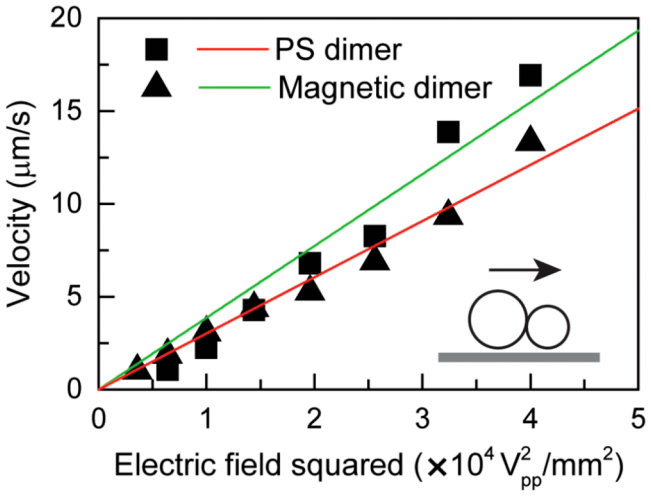

Figure 8. Electrohydrodynamic propulsion velocities of bare PS dimers and SiO_2/Fe_3O_4@PS dimers under different electric field strength (f_E = 400 Hz). The inset shows the dimer propulsion direction.

both bare PS dimers and magnetic dimers scale linearly with the electric field strength squared; i.e., $u \propto E^2$. This trend is consistent with the theoretical prediction from a nonlinear electrokinetic model detailed in our previous publications.[10,11] Briefly, the vertically applied electric field induces mobile charges near the bottom electrode and polarizes both lobes. The polarized lobes themselves generate tangential electric fields that act on the induced charges near the electrode and drive electrohydrodynamic flow surrounding each lobe. If the particle is symmetric, the flow will be balanced, and no particle motion will be observed. The two lobes in our dimer, however, are of different sizes. As a result, the electrohydrodynamic flow surrounding each lobe is unbalanced and leads to net particle propulsion along its long axis. In this case, its small lobe is leading forward, consistent with what we have observed for asymmetric PS dimers[10] and predicted in the theoretical model.[11]

Although the dimer propels in directions perpendicular to the applied electric field, i.e., along the substrate, its moving direction is uncontrolled. Depending on its initial orientation and Brownian motion, its trajectory is not always linear. This leads to difficulty controlling its propulsion direction solely on the basis of the electric field and motivates us to superimpose a magnetic field to control the dimer's orientation.

Controlled Motion of Dimers under Orthogonally Applied Electric and Magnetic Fields. After confirming that our dimers can be driven by the electric field and rotated by the magnetic field, we further investigate the controlled motion of dimers under both fields. In principle, the electric field can generate an unbalanced electrohydrodynamic flow surrounding the asymmetric dimers and provide propulsion power like an engine. On the other hand, the magnetic field can control the dimer orientation by aligning its long axis with the field, which functions as a steering wheel. Therefore, our dimers should behave like a microcar the speed and direction of which can be independently controlled by combining both fields.

As a proof of concept, we use the setup shown in Figure 1. The activation and current input to each coil is controlled by a Matlab code and a data card. For example, when a DC magnetic field pointing toward the positive *x*-axis is needed, a DC current will pass through the coil on the right. A DC magnetic field along any direction in the *x*−*y*-plane can then be generated by passing different currents through one coil in the *x*-direction and a second coil in the *y*-direction, where the ratio of the two currents determines the field direction since any field vector can be decomposed into two basis vectors along *x*- and *y*-directions, respectively. We emphasize here that the overall strength of the DC magnetic field will be kept high so that the dimer quickly responds to the field, aligns its long axis with the field, and maintains the desired orientation. On the other hand, the electric field strength will be used to adjust the propulsion speed. Consequently, we can direct the particle motion with a predefined trajectory by preprogramming the time sequences of when and how long a magnetic field with specific directions needs to be turned on in our Matlab code. In Figure 9a and SI

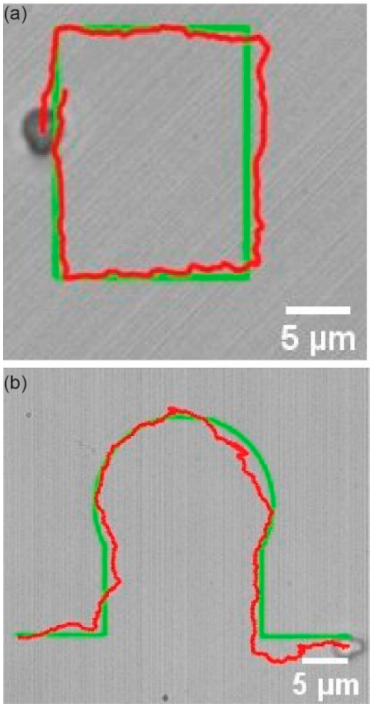

Figure 9. (a) The rectangular-shaped trajectory of a SiO_2/Fe_3O_4@PS dimer drawn by combined fields (8 V_{pp}, 400 Hz electric field, and 1.1 mT DC magnetic field). (b) The omega-shaped trajectory of a SiO_2/Fe_3O_4@PS dimer drawn by combined fields (12 V_{pp}, 1000 Hz electric field, and 1.1 mT DC magnetic field). The red lines represent the particle trajectories and the green lines are designed pathways.

Movie 3a, we show a 20 × 16 μm^2 rectangular-shaped trajectory drawn by the dimer, which was achieved by activating and deactivating four coils sequentially with the same magnitude of the current. Curved trajectories can also be drawn. By splitting a curve into small segments of straight lines, we can direct the particle with an omega-shaped trajectory, as shown in Figure 9b and SI Movie 3b. Both trajectories demonstrate our ability to control particle motion precisely by combining both fields. In our experiments, we noticed that the particles could align both

https://doi.org/10.1021/acs.langmuir.1c01329
Langmuir 2021, 37, 9151−9161

parallelly and antiparallelly with the magnetic field direction since they are energetically equivalent. In practice, the particle, however, tends to align with the direction that requires less rotation. Therefore, a sharp turn with an acute angle is difficult but can be achieved by turning the dimer gradually with a sequence of smaller acute angles.

In addition to linear translation, circular motion can also be achieved by applying an AC electric field along the z-direction and a rotating magnetic field along the $x-y$-plane simultaneously (SI Movie 4). The particle trajectory radius can be further tuned since the dimer's linear velocity, V, is proportional to the electric field strength squared; i.e., $V = aE^2$, where a is a proportional constant that can be determined from Figure 8. The angular velocity, ω_d, is proportional to both χ'' and H_0^2 based on eq 18. Therefore, one can calculate the radius theoretically by

$$R = \frac{V}{\omega_d} = \frac{aE^2 3c\eta(R_1 + R_2)^3}{4\mu_0(R_1^3 + R_2^3)H_0^2\chi''} \quad (19)$$

As shown in Figure 10, we plot the measured particle trajectory radius vs the theoretical prediction for different combinations of electric and magnetic fields, which match very well.

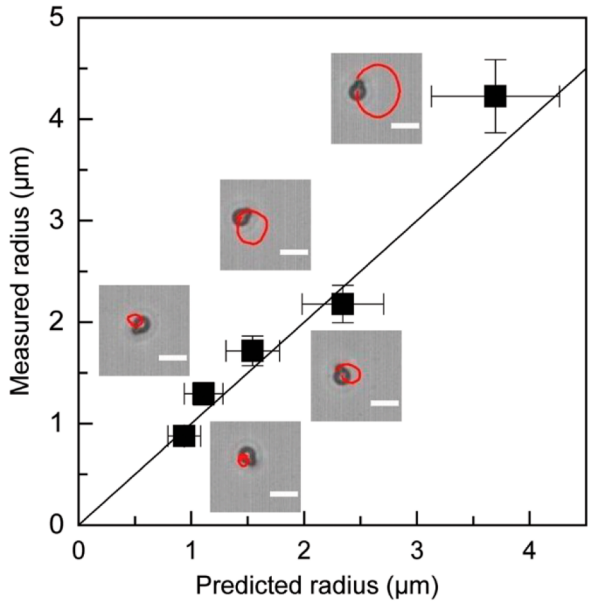

Figure 10. Comparison between the measured and predicted radii of cyclic trajectories of SiO_2/Fe_3O_4@PS dimers under combined $x-y$ rotating magnetic field and z electric field. The solid line with slope 1 is to guide the eye. The insets show the dimer trajectories. The field conditions are 20 V_{pp} + 2.158 mT, 12 V_{pp} + 1.07 mT, 20 V_{pp} + 3.194 mT, 16 V_{pp} + 2.158 mT, and 20 V_{pp} + 2.158 mT to yield small to large radii. The electric field frequency is 400 Hz and the magnetic field frequency is 50 Hz. Scale bars: 5 μm.

Our method of combining electric and magnetic fields allows the control of particle rotation and the radius of its trajectories. In the literature, an AC electric field[41] can induce the helical motion of Janus particles due to induced-charge electrophoresis. In comparison, a rotating magnetic field[42] can cause the rolling and spinning of ferromagnetic particles. In addition, self-diffusiophoretic Janus particles can also rotate at the air−water interface in the presence of hydrogen peroxide.[43] However, the circular (clockwise vs counterclockwise) motion based on the mechanisms mentioned above highly depends on the initial particle orientation. Moreover, the speed of motion is coupled with the trajectory radius. Here, the trajectories can be deterministically controlled by the direction of the rotating magnetic field, while the electric field strength primarily governs the speed. Therefore, our method allows more precise manipulation.

CONCLUSION

We report a new bulk-synthesis strategy to make monodisperse magnetic dimers with geometric anisotropy. This work is accomplished by first coating dopamine-functionalized magnetite nanoparticles and then a thin layer of silica on polystyrene dimers based on electrostatic attraction and heterogeneous nucleation. We further characterized the static and dynamic susceptibilities of those dimers by measuring both magnetic hysteresis diagrams and their rotation speeds under AC magnetic fields. While our dimers' saturation magnetization is 1 order of magnitude smaller than the commercially available Dynabeads, their rotational speeds under AC magnetic fields are similar. The dimer's rotation is primarily driven by permanent dipoles at low frequencies and the imaginary component of the complex magnetic susceptibility at high frequencies. Our method can make other types of magnetically anisotropic particles that are useful in colloidal assembly, micromachines, and particulate emulsifiers.

In addition to chemical synthesis, we further showed that these magnetic dimers responded to electric and magnetic fields independently. While the dimer's orientation can be controlled by a DC magnetic field along the $x-y$-plane, its propulsion speed is solely controlled by the AC electric field applied in the z-direction. Combining both fields, we demonstrated a precise control of the dimer's trajectory by preprogramming the DC magnetic field along with x- and y-directions, respectively, via a Matlab code. Our work demonstrates a simple method to control the orientation and speed of micromotors independently and paves the way for the assembly of magnetically anisotropic particles that can be simultaneously controlled by electric and magnetic fields.

ASSOCIATED CONTENT

Supporting Information

The Supporting Information is available free of charge at https://pubs.acs.org/doi/10.1021/acs.langmuir.1c01329.

SEM images and EDX element analysis of dimers, FC−ZFC curve of dimers, and captions describing SI Movies 1−4 (PDF)

SI Movie 1 (AVI)

SI Movie 2 (AVI)

SI Movie 3 (AVI)

SI Movie 4 (AVI)

AUTHOR INFORMATION

Corresponding Author

Ning Wu − *Department of Chemical and Biological Engineering, Colorado School of Mines, Golden, Colorado 80401, United States;* orcid.org/0000-0002-2167-3621; Email: ningwu@mines.edu

https://doi.org/10.1021/acs.langmuir.1c01329
Langmuir 2021, 37, 9151−9161

Authors

Xingrui Zhu − *Department of Chemical and Biological Engineering, Colorado School of Mines, Golden, Colorado 80401, United States*

Yan Gao − *Department of Metallurgical and Material Science, Colorado School of Mines, Golden, Colorado 80401, United States*

Ramona Mhana − *Department of Chemical and Biological Engineering, Colorado School of Mines, Golden, Colorado 80401, United States*

Tao Yang − *Department of Chemical and Biological Engineering, Colorado School of Mines, Golden, Colorado 80401, United States*

Benjamin L. Hanson − *Department of Physics, Colorado School of Mines, Golden, Colorado 80401, United States*

Xingfu Yang − *Department of Chemical and Biological Engineering, Colorado School of Mines, Golden, Colorado 80401, United States;* orcid.org/0000-0002-0004-0550

Jingjing Gong − *Department of Chemical and Biological Engineering, Colorado School of Mines, Golden, Colorado 80401, United States*

Complete contact information is available at: https://pubs.acs.org/10.1021/acs.langmuir.1c01329

Notes

The authors declare no competing financial interest.

■ ACKNOWLEDGMENTS

This work was supported by the National Science Foundation (CBET-1454095 and ECCS-1611330). We also thank Nan Jiang for his help writing the Matlab code to analyze the particle propulsion trajectories.

■ REFERENCES

(1) Gao, W.; Pei, A.; Feng, X.; Hennessy, C.; Wang, J. Organized Self-Assembly of Janus Micromotors with Hydrophobic Hemispheres. *J. Am. Chem. Soc.* **2013**, *135*, 998−1001.

(2) Khoee, S.; Nouri, A. Preparation of Janus Nanoparticles and Its Application in Drug Delivery. In *Design and Development of New Nanocarriers*; Grumezescu, A. M., Ed.; William Andrew Publishing, 2018; pp 145−180.

(3) Gao, W.; Feng, X.; Pei, A.; Gu, Y.; Li, J.; Wang, J. Seawater-Driven Magnesium Based Janus Micromotors for Environmental Remediation. *Nanoscale* **2013**, *5*, 4696−4700.

(4) Ma, F.; Wang, S.; Wu, D. T.; Wu, N. Electric-Field-Induced Assembly and Propulsion of Chiral Colloidal Clusters. *Proc. Natl. Acad. Sci. U. S. A.* **2015**, *112*, 6307−6312.

(5) Lan, Y.; Choi, J.; Li, H.; Jia, Y.; Huang, R.; Stebe, K. J.; Lee, D. Janus Particles with Varying Configurations for Emulsion Stabilization. *Ind. Eng. Chem. Res.* **2019**, *58*, 20961−20968.

(6) Howse, J. R.; Jones, R. A. L.; Ryan, A. J.; Gough, T.; Vafabakhsh, R.; Golestanian, R. Self-Motile Colloidal Particles: From Directed Propulsion to Random Walk. *Phys. Rev. Lett.* **2007**, *99*, 048102.

(7) Paxton, W. F.; Baker, P. T.; Kline, T. R.; Wang, Y.; Mallouk, T. E.; Sen, A. Catalytically Induced Electrokinetics for Motors and Micropumps. *J. Am. Chem. Soc.* **2006**, *128*, 14881−14888.

(8) Jiang, H. R.; Yoshinaga, N.; Sano, M. Active Motion of a Janus Particle by Self-Thermophoresis in a Defocused Laser Beam. *Phys. Rev. Lett.* **2010**, *105*, 268302.

(9) Gangwal, S.; Cayre, O. J.; Bazant, M. Z.; Velev, O. D. Induced-Charge Electrophoresis of Metallodielectric Particles. *Phys. Rev. Lett.* **2008**, *100*, 058302.

(10) Ma, F.; Yang, X.; Zhao, H.; Wu, N. Inducing Propulsion of Colloidal Dimers by Breaking the Symmetry in Electrohydrodynamic Flow. *Phys. Rev. Lett.* **2015**, *115*, 208302.

(11) Yang, X.; Wu, N. Change the Collective Behaviors of Colloidal Motors by Tuning Electrohydrodynamic Flow at the Subparticle Level. *Langmuir* **2018**, *34*, 952−960.

(12) Ma, F.; Wang, S.; Zhao, H.; Wu, D. T.; Wu, N. Colloidal Structures of Asymmetric Dimers via Orientation-Dependent Interactions. *Soft Matter* **2014**, *10*, 8349−8357.

(13) Hosein, I. D.; Lee, S. H.; Liddell, C. M. Dimer-Based Three-Dimensional Photonic Crystals. *Adv. Funct. Mater.* **2010**, *20*, 3085−3091.

(14) Liang, X.; Mou, F.; Huang, Z.; Zhang, J.; You, M.; Xu, L.; Luo, M.; Guan, J. Hierarchical Microswarms with Leader-Follower-Like Structures: Electrohydrodynamic Self-Organization and Multimode Collective Photoresponses. *Adv. Funct. Mater.* **2020**, *30*, 1908602.

(15) Ebbens, S. J.; Howse, J. R. Direct Observation of the Direction of Motion for Spherical Catalytic Swimmers. *Langmuir* **2011**, *27*, 12293−12296.

(16) Lin, C. H.; Chen, Y. L.; Jiang, H. R. Orientation-Dependent Induced-Charge Electrophoresis of Magnetic Metal-Coated Janus Particles with Different Coating Thicknesses. *RSC Adv.* **2017**, *7*, 46118−46123.

(17) Magdanz, V.; Sanchez, S.; Schmidt, O. G. Development of a Sperm-Flagella Driven Micro-Bio-Robot. *Adv. Mater.* **2013**, *25*, 6581−6588.

(18) Mou, F.; Pan, D.; Chen, C.; Gao, Y.; Xu, L.; Guan, J. Micromotors: Magnetically Modulated Pot-Like MnFe 2 O 4 Micromotors: Nanoparticle Assembly Fabrication and Their Capability for Direct Oil Removal (Adv. Funct. Mater. 39/2015). *Adv. Funct. Mater.* **2015**, *25*, 6173−6181.

(19) Yang, T.; Tomaka, A.; Tasci, T. O.; Neeves, K. B.; Wu, N.; Marr, D. W. M. Microwheels on Microroads: Enhanced Translation on Topographic Surfaces. *Science Robotics* **2019**, *4*, No. eaaw9525.

(20) Yang, T.; Tasci, T. O.; Neeves, K. B.; Wu, N.; Marr, D. W. M. Magnetic Microlassos for Reversible Cargo Capture, Transport, and Release. *Langmuir* **2017**, *33*, 5932−5937.

(21) Singh, G.; Chan, H.; Udayabhaskararao, T.; Gelman, E.; Peddis, D.; Baskin, A.; Leitus, G.; Král, P.; Klajn, R. Magnetic Field-Induced Self-Assembly of Iron Oxide Nanocubes. *Faraday Discuss.* **2015**, *181*, 403−421.

(22) Ranzoni, A.; Janssen, X. J. A.; Ovsyanko, M.; Van IJzendoorn, L. J.; Prins, M. W. J. Magnetically Controlled Rotation and Torque of Uniaxial Microactuators for Lab-on-a-Chip Applications. *Lab Chip* **2010**, *10*, 179−188.

(23) Wang, S.; Wu, N. Selecting the Swimming Mechanisms of Colloidal Particles: Bubble Propulsion versus Self-Diffusiophoresis. *Langmuir* **2014**, *30*, 3477−3486.

(24) An, P.; Zuo, F.; Wu, Y. P.; Zhang, J. H.; Zheng, Z. H.; Ding, X. B.; Peng, Y. X. Fast Synthesis of Dopamine-Coated Fe 3O 4 Nanoparticles through Ligand-Exchange Method. *Chin. Chem. Lett.* **2012**, *23*, 1099−1102.

(25) Wang, S.; Ma, F.; Zhao, H.; Wu, N. Bulk Synthesis of Metal-Organic Hybrid Dimers and Their Propulsion under Electric Fields. *ACS Appl. Mater. Interfaces* **2014**, *6*, 4560−4569.

(26) Kim, H.; Furst, E. M. Magnetic Properties, Responsiveness, and Stability of Paramagnetic Dumbbell and Ellipsoid Colloids. *J. Colloid Interface Sci.* **2020**, *566*, 419−426.

(27) Fonnum, G.; Johansson, C.; Molteberg, A.; Mørup, S.; Aksnes, E. Characterisation of Dynabeads® by Magnetization Measurements and Mössbauer Spectroscopy. *J. Magn. Magn. Mater.* **2005**, *293*, 41−47.

(28) Ngo, T. H.; Tran, D. L.; Do, H. M.; Tran, V. H.; Le, V. H.; Nguyen, X. P. Facile and Solvent-Free Routes for the Synthesis of Size-Controllable Fe3O4 Nanoparticles. *Adv. Nat. Sci.: Nanosci. Nanotechnol.* **2010**, *1*, 035001.

(29) Kim, D. K.; Mikhaylova, M.; Zhang, Y.; Muhammed, M. Protective Coating of Superparamagnetic Iron Oxide Nanoparticles. *Chem. Mater.* **2003**, *15*, 1617−1627.

(30) Hieu, N. M.; Nam, N. H.; Huyen, N. T.; Van Anh, N. T.; Nghia, P. T.; Khoa, N. B.; Toan, N. L.; Luong, N. H. Synthesis of SiO2-Coated Fe3O4 Nanoparticles Using Ultrasound and Its Application in DNA

Extraction from Formalin-Fixed, Paraffin-Embedded Human Cancer Tissues. *J. Electron. Mater.* **2017**, *46*, 3738−3747.
(31) Kodama, R. H.; Berkowitz, A. E.; McNiff, E. J., Jr.; Foner, S. Surface Spin Disorder in NiFe2O4 Nanoparticles. *Phys. Rev. Lett.* **1996**, *77*, 394−397.
(32) Socoliuc, V.; Bica, D.; Vekas, L. Estimation of Magnetic Particle Clustering in Magnetic Fluids from Static Magnetization Experiments. *J. Colloid Interface Sci.* **2003**, *264*, 141−147.
(33) Maldonado-Camargo, L.; Torres-Díaz, I.; Chiu-Lam, A.; Hernández, M.; Rinaldi, C. Estimating the Contribution of Brownian and Néel Relaxation in a Magnetic Fluid through Dynamic Magnetic Susceptibility Measurements. *J. Magn. Magn. Mater.* **2016**, *412*, 223−233.
(34) Fannin, P. C.; Cohen-Tannoudji, L.; Bertrand, E.; Giannitsis, A. T.; Mac Oireachtaigh, C.; Bibette, J. Investigation of the Complex Susceptibility of Magnetic Beads Containing Maghemite Nanoparticles. *J. Magn. Magn. Mater.* **2006**, *303*, 147−152.
(35) Calero-Diaz Del Castillo, V. L.; Rinaldi, C. Effect of Sample Concentration on the Determination of the Anisotropy Constant of Magnetic Nanoparticles. *IEEE Trans. Magn.* **2010**, *46*, 852−859.
(36) Kim, Y. B.; Jin, H. M. Determination of the First Anisotropy Constant of Uniaxial Anisotropic Material from Initial Susceptibility of Magnetization Hard Direction. *J. Magn. Magn. Mater.* **1998**, *189*, 241−250.
(37) Fannin, P. C.; Malaescu, I.; Marin, C. N. The Effective Anisotropy Constant of Particles within Magnetic Fluids as Measured by Magnetic Resonance. *J. Magn. Magn. Mater.* **2005**, *289*, 162−164.
(38) Coughlan, A. C. H.; Bevan, M. A. Rotating Colloids in Rotating Magnetic Fields: Dipolar Relaxation and Hydrodynamic Coupling. *Phys. Rev. E: Stat. Phys., Plasmas, Fluids, Relat. Interdiscip. Top.* **2016**, *94*, 042613.
(39) Pease, C.; Wijesinghe, H. S.; Etheridge, J.; Pierce, C. J.; Sooryakumar, R. Magnetic and Hydrodynamic Torques: Dynamics of Superparamagnetic Bead Doublets. *J. Magn. Magn. Mater.* **2018**, *466*, 323−332.
(40) Strogatz, S. H. *Nonlinear Dynamics and Chaos*; CRC Press: Boca Raton, FL, 2018; Vol. 2, pp 95−115.
(41) Lee, J. G.; Brooks, A. M.; Shelton, W. A.; Bishop, K. J. M.; Bharti, B. Directed Propulsion of Spherical Particles along Three Dimensional Helical Trajectories. *Nat. Commun.* **2019**, *10*, 2575.
(42) Kaiser, A.; Snezhko, A.; Aranson, I. S. Flocking Ferromagnetic Colloids. *Science Advances* **2017**, *3*, e1601469.
(43) Wang, X.; In, M.; Blanc, C.; Würger, A.; Nobili, M.; Stocco, A. Janus Colloids Actively Rotating on the Surface of Water. *Langmuir* **2017**, *33*, 13766−13773.

https://doi.org/10.1021/acs.langmuir.1c01329
Langmuir 2021, 37, 9151−9161